Water Science & Technology

IWA PUBLISHING

Water Science & Technology Vol 88 No 8, 2174 doi: 10.2166/wst.2023.326

Epsilon-MnO_2 simply prepared by redox precipitation as an efficient catalyst for ciprofloxacin degradation by activating peroxymonosulfate

Xiaoyan Li[a,b], Hongbin Zhang[c], Guozhen Zhang[a,*], Tianhong Zhou[a] and Rui Min[a]

[a] School of Environment and Municipal Engineering, Lanzhou Jiaotong University, 88 Anningxi Road, Anning District, Lanzhou City, Gansu Province 730070, China
[b] School of Civil Engineering, Lanzhou University of Technology, 287 Langongping Road, Qilihe District, Lanzhou City, Gansu Province 730050, China
[c] CSCEC AECOM CONSULTANTS CO., LTD, 459 Dingxi Road, Chengguan District, Lanzhou City, Gansu Province 730030, China
*Corresponding author. E-mail: zhangguozhen@mail.lzjtu.cn

GZ, 0000-0002-8837-7982

ABSTRACT

Four kinds of manganese oxides were successfully prepared by hydrothermal and redox precipitation methods, and the obtained oxides were used for CIP removal from water by activating PMS. The microstructure and surface properties of four oxides were systematically characterized. The results showed that ε-MnO_2 prepared by the redox precipitation method had large surface area, low crystallinity, high surface Mn(III)/Mn(IV) ratio and the highest activation efficiency for PMS, that is, when the concentration of PMS was 0.6 g/L, 0.2 g/L ε-MnO_2 could degrade 93% of CIP within 30 min. Multiple active oxygen species, such as sulfate radical, hydroxyl radical and singlet oxygen, were found in CIP degradation, among which sulfate radical was the most important one. The degradation reaction mainly occurred on the surface of the catalyst, and the surface hydroxyl group played an important role in the degradation. The catalyst could be regenerated *in situ* through the redox reaction between Mn^{4+} and Mn^{3+}. The ε-MnO_2 had the advantages of simple preparation, good stability and excellent performance, which provided the potential for developing new green antibiotic removal technology.

Key words: ciprofloxacin, degradation, manganese (hydroxyl) oxide, peroxymonosulfate, reactive oxygen species

HIGHLIGHTS

- Epsilon-MnO_2 nanoflowers were simply prepared by the redox precipitation method.
- Epsilon-MnO_2 nanoflowers were used to activate PMS to degrade CIP in water.
- The high activity of ε-MnO_2 was due to its large surface area, low crystallinity and high surface Mn(III)/Mn(IV) ratio.
- The –OH groups on the surface could promote the activation of PMS.

GRAPHICAL ABSTRACT

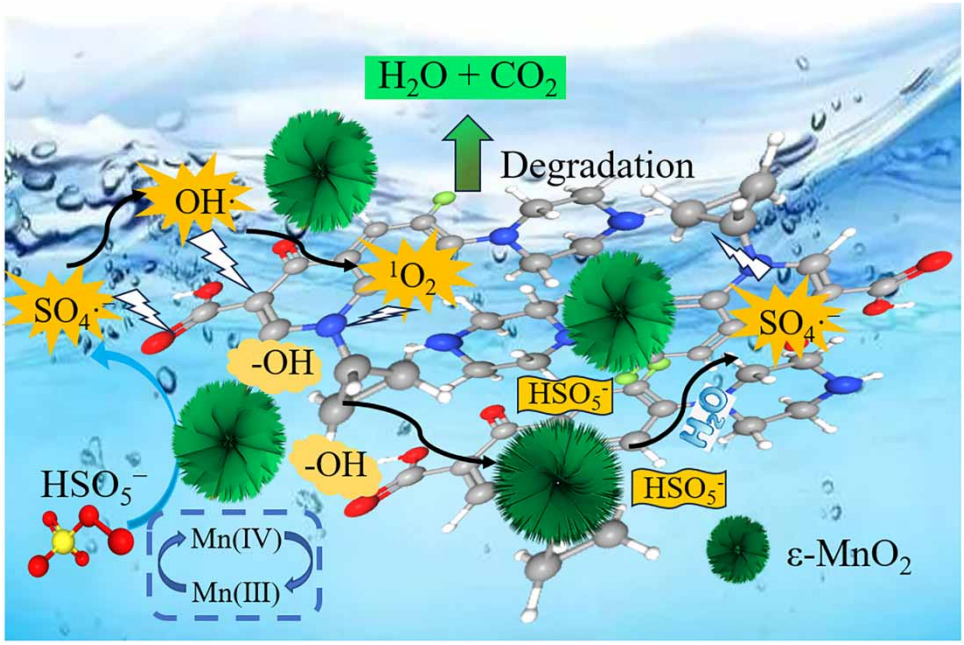

INTRODUCTION

Ciprofloxacin (CIP) is one of the third-generation fluoroquinolone antibiotics. Due to its good clinical efficacy and strong antibacterial activity, it has become one of the most commonly prescribed antibiotics in medicine (Anirudh Gupta 2019; Alhaddad & Amin 2022; Enyoh & Wang 2023). However, more than 75% of CIP cannot be absorbed by humans and animals, resulting in a large amount of CIP residues being released into the water environment (Huang *et al.* 2018a). Recently, it has been detected frequently in surface water, groundwater and even drinking water, with the CIP concentrations ranging from ng L^{-1} to mg L^{-1} (Chun-Hui Shen 2019; Hu *et al.* 2020; Omuferen *et al.* 2022). Unfortunately, due to the poor biodegradability and high ecotoxicity of CIP, it is impossible to effectively remove it from water treatment by various traditional sewage technologies. In recent years, it has been found that the emergence of antibiotic-resistant bacteria and resistant genes due to the extensive use of antibiotics will pose a severe threat to human health and ecosystem security (Yu *et al.* 2020; Falyouna *et al.* 2022). When the World Health Organization revised antibiotic drugs in 2017, it classified some antibiotics as 'prudent use' in an attempt to reduce their use. In addition to effective control at the source, developing treatment technologies to remove such antibiotics from water and wastewater systems is essential.

At present, various methods have been investigated to reduce CIP from water, such as membrane filtration (Nasrollahi *et al.* 2022), adsorption (Arif *et al.* 2022), biodegradation (Shah *et al.* 2022) and advanced oxidation process (AOP) (Salari *et al.* 2022). Among them, the AOP based on sulfate radical has aroused much concern in recent years due to its advantages of economy, high efficiency, environmental protection, safety and stability (Tian *et al.* 2022). Persulfate (PS) includes peroxymonosulfate (PMS) and peroxydisulfate (PDS), both of which contain –O–O– bonds in their molecules. The method for activating PS degradation is to couple and excite PS through specific physical or chemical approaches to break its –O–O– bond and produce strong oxidizing $SO_4^{-\bullet}$, which reacts with organic substances through dehydrogenation, electron addition, electron transfer and other ways to trigger a series of free radical chain reactions, to realize the oxidative degradation of organic pollutants. Currently, PS can be activated in various ways, such as UV activation (Ghauch *et al.* 2017), thermal activation (He *et al.* 2021a), ultrasonic activation (Gujar *et al.* 2023), transition metal ion activation (Fe^{2+}, Mn^{2+}, Cu^{2+}, Ag^{+}, Co^{2+}, Ce^{3+}, etc.) (Huang *et al.* 2009; Gao *et al.* 2018; Yoon *et al.* 2022) and heterogeneous catalysts activation (Tian *et al.* 2022; Zhou *et al.* 2023). UV activation, thermal activation and ultrasonic activation all require external energy. Transition metal ion activation has difficulties in recovery and secondary pollution. In contrast, heterogeneous catalytic materials have become a research hotspot due to their high efficiency, low cost and low energy consumption (Zhang *et al.* 2021).

Transition metal-based heterogeneous materials have been reported to be effective in activating persulfates (Rama *et al.* 2018; Wang & Wang 2018), but cobalt-based or copper-based materials may cause health hazards due to the immersion of toxic ions in the aqueous phase, silver-based materials are expensive, which will limit their practical application. In contrast, manganese-based materials have obvious advantages such as many valence states, high oxygen migration efficiency, abundant resources, low price, friendly environment and strong safety (Huang & Zhang 2019). Manganese oxide has been reported as an effective catalyst for ozone oxidation (He *et al.* 2021b; Issaka *et al.* 2022) and also exhibited excellent performance in catalytic degradation of pollutants by hydrogen peroxide (Hussain *et al.* 2021; Zhen *et al.* 2023).

The synthesis route was of great importance to the physical and chemical properties and structural performance of the catalyst. For decades, a series of synthesis techniques have been used to synthesize manganese oxides, such as hydrothermal (Wang *et al.* 2015a), solvothermal (Ren *et al.* 2014), sol–gel (Zhang *et al.* 2019), template (Huang *et al.* 2018b) and redox precipitation (Wei *et al.* 2023) methods. Hydrothermal and solvothermal synthesis was characterized by high pressure, long period and strict requirements for reactants. There were many steps and uncontrollable factors in the process of sol–gel synthesis, which was difficult to industrialize; The purity of the products synthesized by the template method was not high, and the selection of template agent was very demanding. These shortcomings limited the practical application of many manganese oxides. The synthesis method with high efficiency, low cost and simple operation has become an urgent problem to be solved in the development of new manganese oxide catalysts. Redox precipitation method effectively avoided complex working procedures and special equipment requirements, and it was worth studying because of its simple process, fast reaction speed and diverse morphology of samples.

In recent years, manganese oxides, such as MnO_2, Mn_3O_4 and MnO(OH), have attracted much attention in the field of catalysts because of their physical and chemical properties. Wang *et al.* (2015b) found that α-MnO_2 showed shape dependence when used to degrade phenol; Saputra *et al.* (2013b) concluded through research that Mn_3O_4 had better performance than Fe_3O_4 and Co_3O_4 in activating PMS to degrade pollutants. He *et al.* (2020) synthesized MnO(OH) with the same crystal structure to degrade 2,4-dichlorophenol and found that different morphologies would lead to different physical and chemical properties, thus providing guidance for rational design of catalysts. However, there were few studies on the activity of a series of manganese oxides with different crystal structures in environmental catalysis. At the same time, we also found that the research on MnO_2 was mostly focused on polycrystals. Epsilon-MnO_2 showed low crystallinity due to its own structural fracture (i.e. De Wolff fracture) and structural defect (i.e. micro-twin) (Wang *et al.* 2015a), and its catalytic performance in water treatment was rarely touched.

Herein, four different manganese (hydroxyl) oxides were prepared by hydrothermal and redox coprecipitation methods, and the influence of catalyst structure on catalytic performance was studied by systematic characterization. The degradation of CIP by PMS activated by ε-MnO_2 with low crystallinity was systematically studied to explore the green catalytic materials that were easy to prepare and highly active to degrade antibiotics.

MATERIALS AND METHODS

Materials

All chemicals are used directly after purchase without any treatment. Manganese chloride ($MnCl_2{\cdot}4H_2O$), manganese sulfate ($MnSO_4{\cdot}H_2O$), potassium permanganate ($KMnO_4$), L-histidine ($C_6H_9N_3O_2$) and ciprofloxacin ($C_{17}H_{18}FN_3O_3$) were bought from Shanghai Zhongqin Chemical Reagent Co., Ltd (Shanghai, China). Anhydrous ethanol (CH_3CH_2OH), sulfuric acid (H_2SO_4), methanol (CH_3OH), tert-butanol ($C_4H_{10}O$), sodium hydroxide (NaOH), potassium nitrate (KNO_3), phenol, potassium dihydrogen phosphate (KH_2PO_4), humic acid (HA), sodium chloride (NaCl), sodium carbonate (Na_2CO_3) and nitrobenzol (NB) were provided by Tianjin Damao Chemical Reagent Co., Ltd (Tianjin, China). PMS ($KHSO_5{\cdot}0.5KHSO_4{\cdot}0.5K_2SO_4$, PMS), 5, 5-dimethyl-1-pyrrole Lino-N-oxide (DMPO), 2,2,6,6-tetramethylpiperidine (TEMP) were purchased from Aladdin Reagent Co., Ltd (Shanghai, China).

Manganese (hydroxyl) oxide synthesis

The valence heterostructure manganese oxides (MnOx) were prepared by hydrothermal method. Typically, 0.79 g (5 mmol) of $KMnO_4$ was dissolved in 50 mL of a mixed solvent of ethanol and water, 0.99 g (5 mmol) of $MnCl_2{\cdot}4H_2O$ was added, stirred for about 30 min until the mixture was uniform and transferred to 100 mL of polytetrafluoroethylene (PTFE) liner stainless steel jacket reactor for 160° hydrothermal treatment for 12 h. The brown precipitates were washed three times with deionized water and anhydrous ethanol, respectively and then dried at 70° C for 24 h. In the experiment, the volume ratio of ethanol and

water in the solvent was adjusted to 0:100, 50:50 and 100:0, respectively, to prepare nanomaterials with different crystal forms and morphologies, which were recorded as MnOx-1, MnOx-2 and MnOx-3.

Manganese oxide (MnOx-4) was synthesized by the redox coprecipitation method. 0.004 mol (0.6321 g) $KMnO_4$ was added to 200 mL of 0.03 mol/L $MnSO_4{\cdot}H_2O$ solution and stirred for 30 min. Afterward, the solution was placed in a collector magnetic stirrer at 75 °C and went for 5 h to obtain a black precipitate. The precipitate was washed for several times alternately with deionized water and anhydrous ethanol until the supernatant was neutral, then it was put into a 60 °C constant temperature drying oven for 24 h after suction filtration and grounded to powder after cooling, which was denoted as MnOx-4.

Characterization

The microstructure of the catalysts was studied by X-ray diffractometer (XRD, X'pert pro) using the scanning angle (2θ) at 10–90° and Cu–Kα radiation at 40 kV and 40 mA. The microtopography of the catalysts was characterized by scanning electron microscopy (SEM, Apreo S) and transmission electron microscope (TEM, FEI Tecnai F 30). The sample elements and surface topography were analyzed using energy-dispersive methods (EDS, EDAX). The chemical bonds and functional groups of the catalysts were measured by a Fourier-transform infrared spectrometer (FTIR, VERTEX 70, Bruker). X-ray photoelectron spectroscopy (XPS, PHI 5702) was mainly used to characterize the elemental composition and valence state of the catalyst surface. The Brunauer–Emmett–Teller (BET) surface areas were determined by N_2 adsorption tester (JW-BK200C). Electron paramagnetic resonance spectroscopy (EPR, Bruker EMX plus) was used to identify free radicals in solution and solid oxygen vacancies. The detection parameters were as follows: microwave frequency 9.8434 GHz, scanning width 100 G, central field 3,505.00 G, modulation amplitude 1 G, time constant 5.12 ms and scanning time 60 s.

Catalytic degradation

The catalytic performance of the prepared four kinds of MnOx was investigated by activating PMS to degrade CIP in water. All degradation experiments were carried out in 250 mL beakers on a constant temperature magnetic stirrer (speed 1,200 rpm). First, a certain amount of catalyst was added to the 200 mL prepared target pollutants (10 $mg{\cdot}L^{-1}$), after the catalyst reached adsorption equilibrium with the solution, a certain amount of PMS was added to start the timing. Five millilitres (5 mL) sample was taken from the beaker at regular intervals, filtered through a 0.45 μm microfiltration membrane and quenched with methanol. The CIP concentration was determined by measuring the absorbance at the maximum absorption wavelength of 277 nm with an ultraviolet spectrophotometer (UV-2800A).

When exploring the influence of different parameters on the degradation of pollutants, the single-variable principle was used for experimental analyses. During the investigation, 0.1 $mol{\cdot}L^{-1}$ H_2SO_4 and NaOH solutions were used to regulate the pH of the solution to study the influence of the initial pH value. To check the effect of quenchers on degradation experiments, MeOH, TBA, L-His, phenol, KH_2PO_4 and NB were selected as quenchers and set blank control at the same time. Samples were taken at regular intervals for testing after the degradation began. To explore the stability and reuse performance of the catalyst, the cyclic degradation test of the catalyst was carried out. After a single reaction, the catalyst was recovered and washed repeatedly, then put into a constant temperature drying oven at 80 °C for drying and reuse.

When the synthesized catalyst was further applied to the removal of CIP from actual water, the raw water obtained from Liujiaxia Reservoir in the upper reaches of the Yellow River was first filtered with 0.45 μm PTFE filter, which was used to dissolve CIP and configured into a solution of target concentration, and the removal effect of ε-MnO_2/PMS on CIP was observed.

RESULT AND DISCUSSION

Catalyst characterization

The crystal structure of the prepared catalyst could be judged by the XRD diffraction pattern of the sample and its matching with the standard pattern Joint Committee on Powder Diffraction Standards (JCPDS). The XRD spectrum of the four manganese oxides is shown in Figure 1(a). It was observed that the change in the content of ethanol in the solvent directly affected the phase of the product. When the solvent was water, the diffraction peaks of MnOx-1 appeared at 2θ of 18.107°, 28.841°, 37.522°, 41.968°, 56.372° and 69.711°, corresponding to (200) (310) (211) (301) (600) and (541) planes of the Tetragonal α-MnO_2 (PDF #44-0141). The diffraction peaks of MnOx-2 prepared by 50% hydrothermal water and 50% ethanol appeared at 2θ of 26.149°, 35.538°, 37.168°, 51.222°, 54.864°, 61.797°, 71.152°, 81.503° and 85.478°, corresponding to Monoclinic γ-MnO(OH) (11-1), (111), (002), (022), (11-3), (131), (113), (2-2-4) and the (242) plane (PDF #41-1379). The diffraction

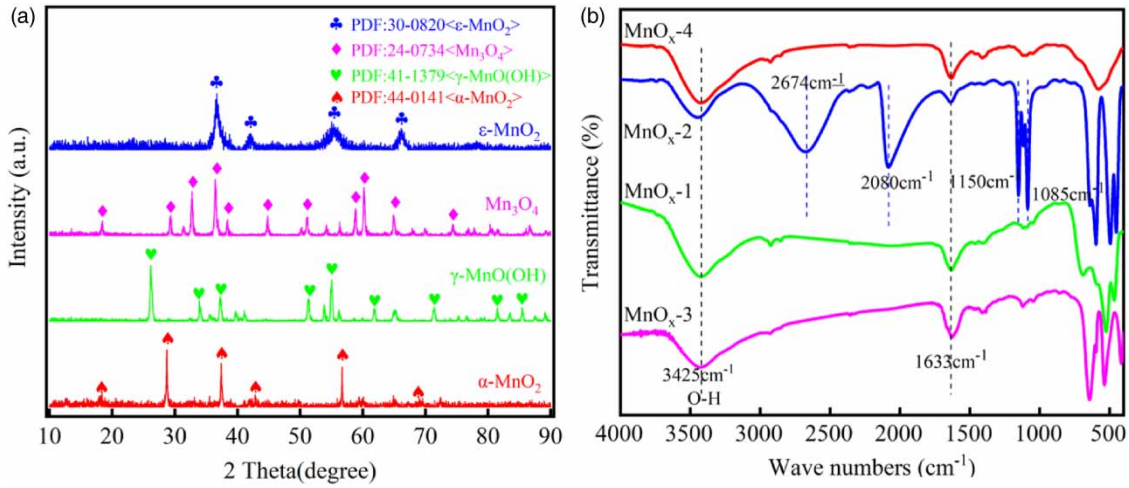

Figure 1 | XRD patterns (a) and FTIR spectra (b) of four manganese (hydrogen) oxides.

peaks of MnOx-3 prepared with ethanol appeared at 2θ of 18.00°, 28.88°, 32.315°, 36.449°, 37.983°, 44.44°, 50.709°, 58.510°, 59.84°, 64.651° and 74.151°, corresponding to Tetragonal Mn_3O_4 (101), (112), (103), (202), (004), (220), (105), (321), (224), (400) and (413) planes (PDF #24-0734). This might be due to the fact that when the solvent was all water, $KMnO_4$ was reduced by Mn^{2+} to MnO_2, as shown in Equation (1). When the solvent was all ethanol, $KMnO_4$ was reduced by ethanol to produce Mn_3O_4, as shown in Equation (2). The production of Mn_3O_4 was accompanied by the production of KOH, and the solution was alkaline. The increase of ethanol in the solvent caused a large amount of OH^- to be generated in the solution, which combined with Mn^{2+} to produce $Mn(OH)_2$. The unstable $Mn(OH)_2$ was rapidly oxidized to MnO(OH) (Mn has a +3 valence). The diffraction peaks of MnOx-4 prepared by the redox coprecipitation method appeared at 2θ of 37.12°, 42.401°, 56.027° and 66.761°, corresponding to (100), (101), (102) and (110) crystal planes of hexagonal ε-MnO_2 (PDF #30-0820), respectively. The diffraction peak positions of the four catalysts could be matched with the PDF card, and there were almost no impurity peaks. The diffraction peaks of the first three manganese oxides were sharp, indicating that the catalyst prepared by the hydrothermal method had good crystallinity, while the fourth catalyst prepared by the redox precipitation method had wide diffraction peaks and low crystallinity.

$$2KMnO_4 + 3MnCl_2 + 2H_2O \rightarrow 5MnO_2 + 2KCl + 4HCl \quad (1)$$

$$6KMnO_4 + 13CH_3CH_2OH \rightarrow 2Mn_3O_4 + 13CH_3CHO + 6KOH + 10H_2O \quad (2)$$

The FTIR of the four manganese oxides is shown in Figure 1(b). It could be seen that the absorption peaks of the four manganese oxides appeared at 3,425 and 1,633 cm^{-1}, which could be related to the stretching vibration and bending vibration of hydroxyl. The absorption peaks of γ-MnO(OH) at 1,150 and 1,085 cm^{-1} were attributed to the bending vibration of hydroxyl, and the absorption peaks at 2,674 and 2,080 cm^{-1} were assigned to the stretching vibration of hydroxyl. This indicated that there were abundant hydroxyl groups on the surface of the four catalysts. The absorption peaks in the 400–800 cm^{-1} corresponded to the vibrational absorption of Mn–O metal bonds in manganese oxides. FTIR showed that the Mn–O metal bonds had been formed in the four catalysts, and a large number of hydroxyl groups existed on the surface of the catalysts.

Figure 2(a)–2(f) shows the morphological characteristics of the four manganese oxides. The α-MnO_2 and γ-MnO(OH) prepared by solvent containing water were both nanorods with smooth surfaces and a small number of nanoparticles. The diameter of the latter was larger than that of the former, which was about 200 nm (Figure 2(b)), and the former was about 50 nm (Figure 2(a)). Combined with XRD, it was speculated that the two rods were α-MnO_2 and γ-MnO(OH). From Figure 2(c), it could be seen that Mn_3O_4 presented nano-spherical particles with uniform particle size, the spherical surface was smooth, the diameter was about 50–100 nm and the particles tended to agglomerate. According to the XRD pattern, it was speculated to be Mn_3O_4 spherical particles. With the increase of the proportion of ethanol in the hydrothermal solvent,

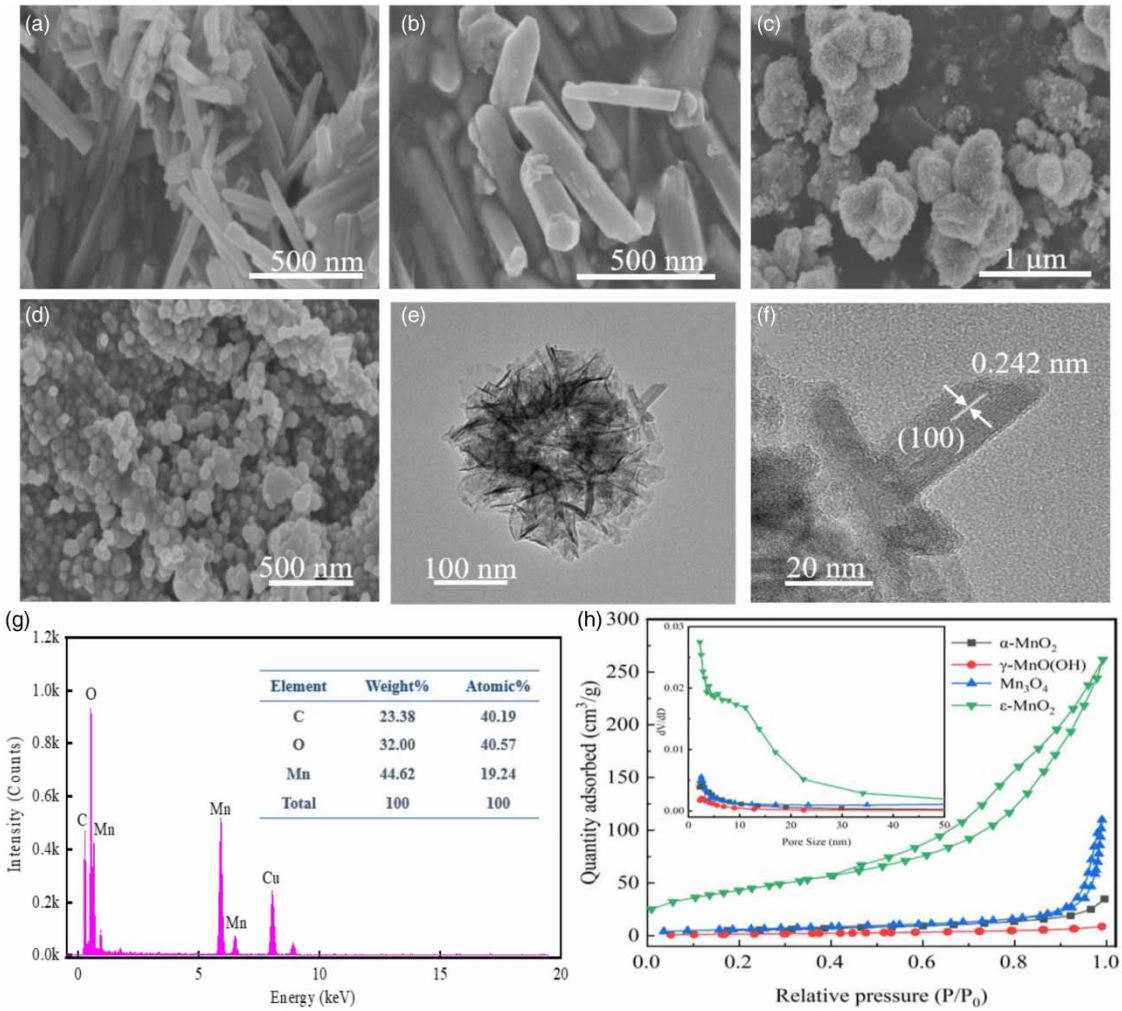

Figure 2 | SEM images of α-MnO_2 (a), γ-MnO(OH) (b), Mn_3O_4 (c), ε-MnO_2 (d), TEM images of ε-MnO_2 (e,f); EDS of ε-MnO_2 (g), N_2 adsorption–desorption isotherms of ε-MnO_2 (h).

the morphology of the catalyst prepared under the same conditions gradually changed from a slender rod to a larger diameter and finally transited to a smaller spherical diameter, with little change in the surface roughness. In these reactions, ethanol not only acted as a solvent to provide the reaction environment, but also participated in the reaction as a reducing agent, thereby affecting the composition, phase and morphology of the products. The surface of ε-MnO_2 was rough in Figure 2(d), showing cluster-like spherical nanoflowers with a small number of nanoparticles attached. The diameter of the nanoflowers was about 1 μm, which was speculated to be ε-MnO_2 in combination with XRD. TEM images (Figure 2(e)) further confirmed the mesoporous nanoflower structure of ε-MnO_2, showing clear lattice streaks in Figure 2(f) with a spacing of 0.242 nm, corresponding to the (100) face of ε-MnO_2. As shown in EDS (Figure 2(g)), ε-MnO_2 nanomaterials were composed of Mn and O elements, and the coexisting element ratio Mn/O was 2.1, which was close to the theoretical stoichiometric value of ε-MnO_2.

According to the measurement of N_2 adsorption and desorption, the four samples in Figure 2(h) presented a typical type-IV isotherm, which indicated that all four catalysts were mesoporous materials with average pore diameters ranging from 2 to 50 nm, and there were obvious H_3-type hysteresis loops between the adsorption and desorption isotherms of Mn_3O_4 and ε-MnO_2 in the range of P/P_0 of 0.4–1.0 and 0.8–1.0, respectively. It could be inferred that these two catalysts were composed of slit-like pores of flaky particles (Yang *et al.* 2001). As shown in Table S1, the BET surface area of ε-MnO_2 was 156.43 m^2/g, which was 8.25 times that of α-MnO_2, 25.35 times of γ-MnO(OH)

and 6.66 times of Mn_3O_4. The pore volume of ε-MnO_2 was 0.42 cm^3/g, which was 7.5 times that of α-MnO_2, 28.49 times of γ-MnO(OH) and 2.43 times of Mn_3O_4.

The elemental composition and valence state of the catalyst were investigated by XPS. It could be seen from the full spectrum diagram of catalyst XPS (Figure 3(a)) that the four catalysts mainly contain two elements, Mn and O (element C comes from the test instrument). The XPS spectrum of Mn $2p_{3/2}$ in the sample is shown in Figure 3(b). The binding energy positions of Mn^{4+}, Mn^{3+} and Mn^{2+} were determined by comparing literatures (Saputra *et al.* 2013b; He *et al.* 2020; Lin & Chen 2020; Liu *et al.* 2021), and the relative contents of Mn in different valence states could be obtained by the proportion of peak areas after peak fitting. The relative contents of Mn^{3+} in α-MnO_2, γ-MnO(OH), Mn_3O_4, ε-MnO_2 were 71.21, 70.68, 21.6 and 85.4%, respectively. The relative contents of Mn^{4+} in α-MnO_2, γ-MnO(OH), Mn_3O_4, ε-MnO_2 were 28.79, 29.32, 5.8 and 14.6%, respectively, and the content of Mn^{2+} in Mn_3O_4 was 72.6%. The XPS spectrum of sample O1s was shown in Figure 3(c), the peaks in 529.0–530.0 eV, 531.0–532.0 eV and around 533 eV belonged to lattice oxygen (O_{latt}), surface adsorbed oxygen (O_{ads}) and surface hydroxyl oxygen ($O_{adsO\text{-}H}$), respectively. The relative content of O_{latt} was 51.03, 26.92, 56.20 and 36.2% in α-MnO_2, γ-MnO(OH), Mn_3O_4 and ε-MnO_2, and the content of O_{ads} was 37.04, 66.53, 43.80 and 63.8%, respectively. $O_{adsO\text{-}H}$ was found only in α-MnO_2 and γ-MnO(OH) with relative contents of 11.93 and 6.55%, respectively.

CIP degradation in different reaction systems

It could be seen from Figure 4(a) that the degradation of CIP by α-MnO_2, γ-MnO(OH), Mn_3O_4 and ε-MnO_2 in the absence of PMS was 28.65, 9.75, 18.71 and 43.66%, respectively, which might be caused by adsorption or direct oxidation. Only 10.53% of CIP was removed in a separate PMS system, indicating that PMS was difficult to degrade pollutants directly. After adding catalysts to the system, the degradation efficiency of α-MnO_2, γ-MnO(OH), Mn_3O_4 and ε-MnO_2 in the PMS system for CIP

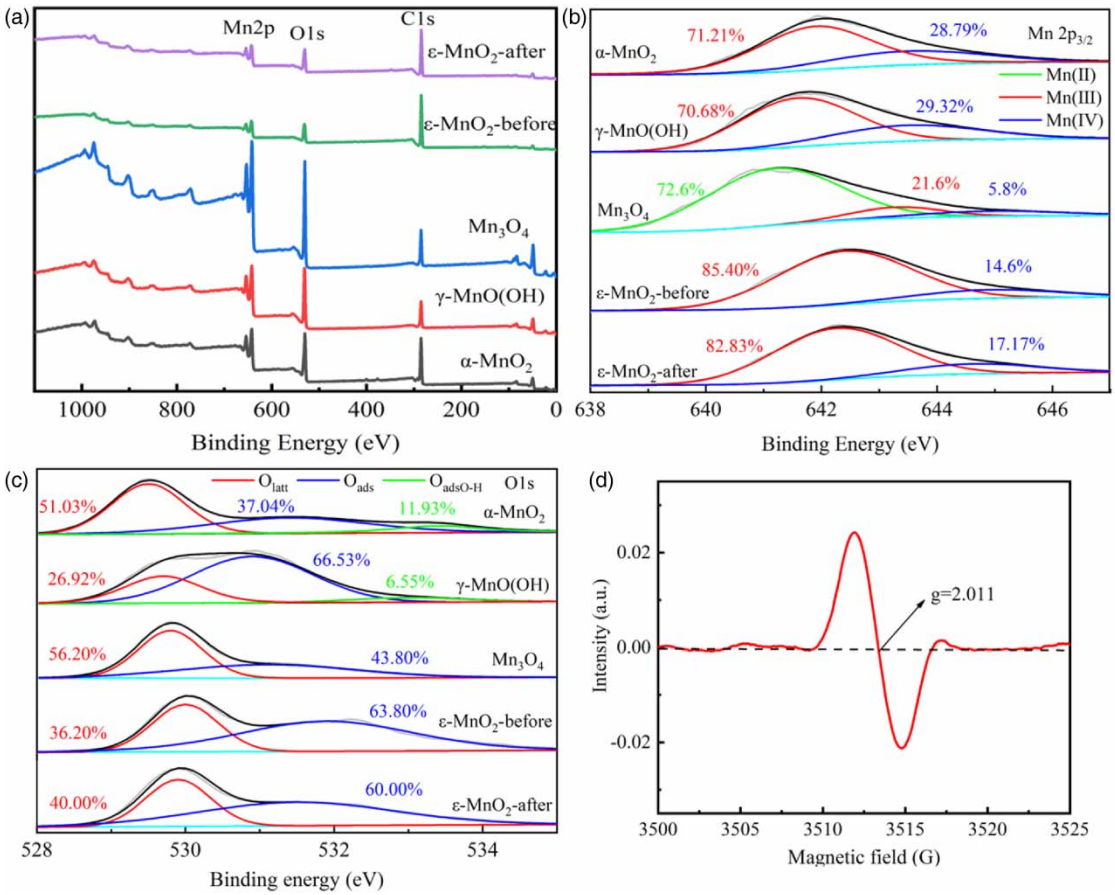

Figure 3 | XPS spectra of survey (a), Mn 2p (b), O 1s (c) of α-MnO_2, γ-MnO(OH), Mn_3O_4 and ε-MnO2 before and after reaction; EPR of ε-MnO_2(d).

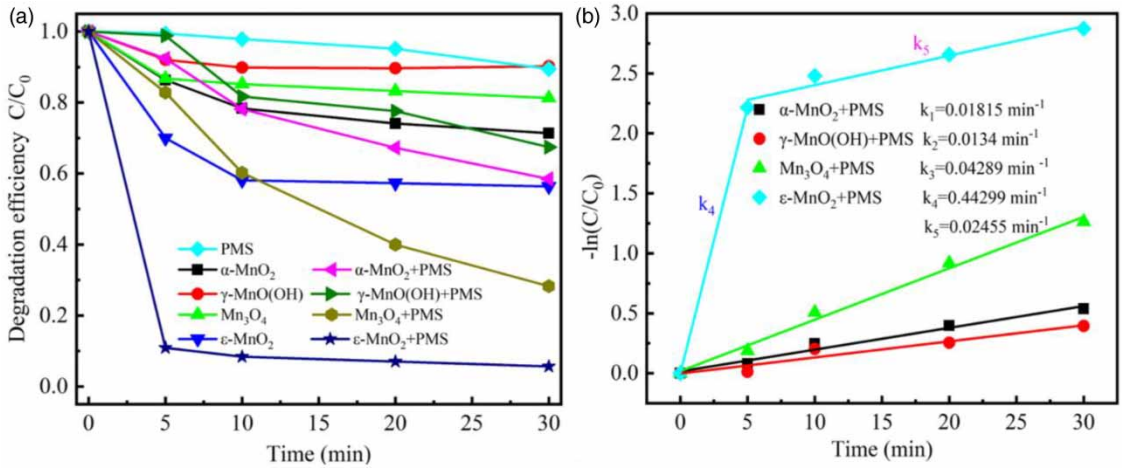

Figure 4 | Degradation of CIP (a) and reaction rate constants (b) in different reaction systems. Reaction conditions: $[CIP]_0 = 10$ mg/L, [catalyst] = 0.2 g/L, [PMS] = 0.6 g/L, temperature = 25 °C, pH was not adjusted.

reached 41.52, 32.55, 71.73 and 94.35%, respectively. ε-MnO_2 also showed excellent activity compared to other MnO_2 in Table S2 that had been reported. All the reaction characteristics conformed to the first-order reaction kinetics ($R^2 > 0.95$) (Figure 4(b)), and the average degradation rate constant k of CIP in ε-MnO_2/PMS system was 0.09429, which was 5.20, 7.04 and 2.2 times higher than that in α-MnO_2/PMS, γ-MnO(OH)/PMS and Mn_3O_4/PMS systems, respectively. The results showed that all four catalysts could activate PMS to degrade pollutants, and ε-MnO_2 had the best effect, which might be related to its structure and surface physicochemical properties.

It has been reported that the catalytic activity of manganese oxides of the same type was affected by the structure, especially the tunnel size and crystallinity (Saputra *et al.* 2013b; Huang *et al.* 2019). For instance, α-MnO_2 with (2×2) tunnel structure had a larger size and higher degradation efficiency than β-MnO_2 with (1×1) tunnel structure and γ-MnO_2 with (1×1) and (1×2) tunnel structure. The four catalysts prepared were α-MnO_2 with (2×2) tunnel structure, γ-MnO(OH) with (1×1) tunnel structure, Mn_3O_4 with spinel-like structure and ε-MnO_2 with (1×1) tunnel and (2×1) tunnel in a matrix of random coexistence, respectively. The degradation efficiency followed the order ε-$MnO_2 > Mn_3O_4 > \alpha$-$MnO_2 > \gamma$-MnO(OH), which was inconsistent with the reported results. It might be that the mesoporous nanostructures of ε-MnO_2 exhibited more active sites due to its defects. The ε-MnO_2 with the highest reaction efficiency was found to have the lowest crystallinity among the four catalysts, which was also different from the conclusions in the literature. Combined with the EPR spectrum of ε-MnO_2 in Figure 3(d), a sharp symmetric peak appears at $g = 2.011$, which could be considered as the solid defect existing in the structure of ε-MnO_2 led to the formation of oxygen vacancy (Zhao *et al.* 2020), thus improving the catalytic activity.

By comparing the SEM of four nanoparticles, it was found that the reactivity of nanorods and spherical nanoparticles was higher than that of nanorods and spherical nanoparticles, which was consistent with the findings of Wang and Jing *et al.* (Wang *et al.* 2015b; Jing *et al.* 2017), that is, the nanoflower shape shows the greatest ability to activate PMS, which was conducive to the heterogeneous reaction on the catalyst surface.

The order of BET surface area and pore volume was ε-$MnO_2 > Mn_3O_4 > \alpha$-$MnO_2 > \gamma$-MnO(OH), which was consistent with the results of CIP degradation by activated PMS. The larger surface area meant more exposed active sites, and the larger void volume could reduce the diffusion resistance, thus showing better adsorption performance and catalytic performance (Liu *et al.* 2020), which was beneficial to the activation of PMS.

In addition, it was reported that Mn(III) content played an important role in Mn-based catalysts (Meng *et al.* 2014), because it was generally believed that $SO_4^{-\bullet}$ was generated by Mn (III) reaction (Equation (3)), while $HSO_5^{-\bullet}$ was generated by Mn (IV) reaction (Equation (4)), and $SO_4^{-\bullet}$ was higher than $HSO_5^{-\bullet}$ oxidation–reduction potential (Wen-Da *et al.* 2016). Unfortunately, the content of Mn(III) in the four catalysts did not show a significant correlation with the degradation efficiency of pollutants. However, it was found that the Mn(III)/Mn(IV) ratio in the catalyst was positively correlated with the degradation

efficiency of CIP, which might be related to the redox reaction occurring during the degradation of manganese oxides.

$$\equiv Mn^{4+} + HSO_5^- \rightarrow Mn^{3+} + SO_5^{-\bullet} + H^+ \quad (3)$$

$$\equiv Mn^{3+} + HSO_5^- \rightarrow Mn^{4+} + SO_4^{-\bullet} + H^+ \quad (4)$$

In summary, it was not difficult to see that the chemical properties and reactivity of manganese oxides were highly dependent on their structure. High BET surface area could provide more reaction sites; ε-MnO_2 with low crystallinity might have the best activation performance because of its own defects leading to the formation of oxygen vacancy. The oxidation capacity of manganese oxides was positively correlated with the ratio of Mn(III)/Mn(IV) content, which might indicate that high Mn(III)/Mn(IV) content could promote the redox reaction in the process of manganese oxides activation of PMS.

Effect of reaction conditions

The process of ε-MnO_2 activating PMS to degrade CIP was influenced by many reaction factors. The effects of catalyst dosage, PMS dosage, initial pH of solution, reaction temperature, common anions in water and actual water on CIP degradation were discussed, and the optimal reaction parameters of the system were determined to provide a reference for engineering practice.

Figure s1a showed when the dosage of ε-MnO_2 was 0.05, 0.1, 0.2, 0.4, 0.6 and 1.0 g·L^{-1}, the degradation efficiencies of CIP after 30 min of reaction reached 66.7, 83.8, 92.4, 95.3, 95.9 and 97.1%, respectively. Obviously, the increase of catalyst concentration could promote the degradation of CIP, because with the increase of catalyst content in the reaction system, more active sites would be generated in the system, and more active components would be produced to remove more CIP. However, when the catalyst dosage was higher than 0.2 g/L, the removal rate of CIP increased slowly. Therefore, 0.2 g/L was selected as the catalyst concentration of the system.

As the source of $SO_4^{-\bullet}$ in the reaction system (Equation (5)), the concentration of PMS would have an immediate impact on the concentration of free radicals and thus the degradation of CIP. In this experiment, the influence of different PMS concentrations on the CIP removal rate was discussed, and the results are shown in Figure s1b. With the concentration of PMS increasing from 0.1 to 0.6 g/L, the removal rate of CIP rose from 69.0 to 90.8% after 30 min of reaction. However, when the concentration of PMS continued to increase to 1.0 g/L, the removal rate of CIP decreased by 0.2%, which was mainly due to the autolysis (Equation (6)) and $SO_4^{-\bullet}$ quenching caused by excess PMS (Equation (7)). Therefore, the concentration of PMS was selected as 0.6 g/L in this experiment.

$$2HSO_5^- + e^- \rightarrow SO_4^{-\bullet} + SO_4^{2-} + H^+ \quad (5)$$

$$SO_4^{-\bullet} + HSO_5^- \rightarrow SO_5^{-\bullet} + SO_4^{2-} + H^+ \quad (6)$$

$$SO_4^{-\bullet} + SO_4^{-\bullet} \rightarrow 2SO_4^{2-} \quad (7)$$

According to relevant literature (Chen *et al.* 2017), AOPs based on $SO_4^{-\bullet}$ had better pH adaptability than traditional AOPs. Therefore, under the conditions of determining the amount of catalyst and PMS, the effect of pH on the degradation of CIP was investigated. As shown in Figure S1c that the ε-MnO_2/PMS system could maintain a high degradation efficiency in the range of pH 2–11, in which more than 90% of CIP could be removed within the range of initial solution pH 3–7, and the removal rate of CIP was close to 90% (85.6 and 88.5%) at pH 2 and 9, indicating that the system had good adaptability in both acidic and weak alkaline environments. When the pH was 11, the removal rate of CIP was reduced to 78.4%. This aspect was that when the PH of the solution was higher than the zero-point charge (PZC) of ε-MnO_2 (Lin & Chen 2020), the surface of ε-MnO_2 was negatively charged, generating charge repulsion with HSO_5^-, which hindered the contact between them and reduced the activity. In addition, the transformation of free radicals (Equation (8)) under alkaline conditions also affected the degradation efficiency. The redox potential of •OH was lower than that of $SO_4^{-\bullet}$, thus reducing the reaction rate. Therefore, ε-MnO_2 could activate PMS under conventional conditions without additional pH adjustment, which provided convenience for practical applications.

$$SO_4^{-\bullet} + OH^- \rightarrow SO_4^{2-} + \bullet OH \quad (8)$$

Figure S1d shows the influence of different temperatures on the degradation of CIP by ε-MnO_2-activated PMS. It could be seen from the figure that the removal rate of CIP increased with the temperature rise. When the reaction temperature was 15, 25 and, 35 °C, the CIP removal rates were 83.5, 90.8 and, 92.0%, respectively, after 30 min reaction. This result could be attributed to the fact that PMS could be decomposed into $SO_4^{-\bullet}$ (Equation (9)) through thermal activation. In addition, high temperatures could speed up the diffusion reaction in the system, thus accelerating the degradation of CIP. The Arrhenius formula (Equation (10)) was used to calculate the activation energy (E_a) of the reaction to estimate the effect of thermal energy. The calculated result was 12.52 kJ mol^{-1}, indicating that the reaction was not only controlled by diffusion but also by heterogeneous chemical reaction. Compared with other manganese-based catalysts for activating PS degradation reactions (as shown in Table s3), the E_a of the ε-MnO_2 reaction was significantly reduced, indicating that the reaction could be carried out under low energy conditions, thus demonstrating its superior catalytic performance.

$$HSO_5^- + \text{heat} \rightarrow SO_4^{-\bullet} + OH\bullet \tag{9}$$

$$\ln k = (\ln A) - E_a/RT \tag{10}$$

where k is the rate constant, the fitting result was displayed in Figure s1d inset. A is the prefactor, R is the gas constant (8.314 J mol^{-1} K^{-1}) and T is the absolute temperature (K).

There were often various inorganic anions and natural organic matter in actual water, such as Cl^-, CO_3^{2-}/HCO_3^-, NO_3^-, etc., which would affect the activation efficiency of PMS by quenching free radicals and competing with the active site of the catalyst. Humic acid (HA) was the most common natural organic matter in water, mainly consisting of aromatic ring, hydroxyl group and phenolic hydroxyl group, which might adsorb on the surface of the material to occupy the active site or compete for free radicals in water, thus affecting the removal effect of pollutants. Figure S1e shows the effect of 5 mmol/L Cl^-, CO_3^{2-}/HCO_3^-, NO_3^- and HA, as well as the Yellow River water as solvents on the degradation of CIP by ε-MnO_2-activated PMS. Only CO_3^{2-}/HCO_3^- and HA among them had inhibitory effects on the system, the other had little effect. As shown in the figure, CO_3^{2-}/HCO_3^- significantly inhibited the degradation of CIP in the system, which might be due to the competitive reaction of both CO_3^{2-}/HCO_3^- and CIP, resulting in the formation of intermediates (Equation (11)) with low or no oxidation performance (Lin & Tsai 2019). In addition, the addition of CO_3^{2-}/HCO_3^- would increase the alkalinity of the solution, which was not conducive to the degradation of CIP according to the research conclusion of the influence of PH value. HA had a certain inhibitory effect on CIP degradation, which might be that HA occupied the active site of MnO_2 and affected its binding with PMS to form reaction intermediates, or that HA competed with CIP to react with active substances, leading to a decrease in CIP degradation efficiency. In addition, ε-MnO_2/PMS also had excellent removal performance in CIP solution with Yellow River water as solvent, which indicated that ε-MnO_2/PMS system had a good application prospect.

$$SO_4^{-\bullet} + HCO_3^- \rightarrow SO_4^{2-} + H^+ + CO_3^{-\bullet} \tag{11}$$

Catalytic stability

In order to explore the stability of the catalyst, the prepared catalyst ε-MnO_2 was tested for cyclic degradation. It was apparent from Figure S2 that ε-MnO_2 was relatively stable and still exhibited excellent catalytic performance after four cycles of degradation experiments. The removal rate of CIP in the fourth cycle in 30 min was 77.4%, 15.7% lower than that in the first cycle. The reasons could be attributed to two aspects: with the increase in catalyst cycle degradation times, the active components on the catalyst surface might be lost, resulting in a gradual reduction of active sites. In addition, the small molecule intermediates generated in the process of organic degradation gathered on the catalyst surface, which hindered the contact of the catalyst with PMS and CIP, thus reducing the removal rate of CIP.

Exploration of the catalytic mechanism

To explore the main reaction active species in the system, tert-butanol (TBA), methanol (MeOH) and L-histidine (L-His) were used as quenchers to investigate the effect of CIP degradation in the ε-MnO_2/PMS system. According to the literature (Hao *et al.* 2019), the reaction rate constants of MeOH and TBA with •OH and $SO_4^{-\bullet}$ were shown in Table s4, in which the reaction

rate constant of MeOH and •OH was 50 times that of $SO_4^{-\bullet}$, while the reaction rate constant of TBA and •OH was 1,000 times that of $SO_4^{-\bullet}$. When the solution contains two free radicals simultaneously, it could be considered that TBA only quenched •OH, while MeOH quenched •OH and $SO_4^{-\bullet}$. The contribution of the two free radicals was judged by comparing the effects of two kinds of quenching agents on the degradation of CIP in the system. L-histidine could be used to quench singlet oxygen ($^1O_2$) (Chen *et al.* 2018) with a second-order rate constant of 3×10^7 (D_2O, pD = 7) (Wilkinsan 1981). So MeOH (3 M), TBA (3 M) and, L-His (0.2 mM) were used to identify the presence of active species such as $SO_4^{-\bullet}$, •OH and, $^1O_2$ in the system, respectively.

As described in Figure 5(a), after TBA was added to the system, the removal rate of CIP decreased from 91.9 to 79.2% 30 min later, indicating the presence of •OH in the system. The CIP removal rate was further reduced to 72.6% after the addition of MeOH, which meant that not only •OH but also $SO_4^{-\bullet}$ existed in the ε-MnO_2/PMS system. Compared with the case of no quencher, the removal rate of CIP decreased by 13.3% after adding L-His to the system, which indirectly indicated that there was still $^1O_2$ in the ε-MnO_2/PMS system to promote the degradation of CIP. The inhibition effect of MeOH on CIP was less than that of TBA, indicating that •OH was not the main free radical in the system. The addition of MeOH could consume the generated $SO_4^{-\bullet}$ and •OH, but these two quenchers had no significant effect on CIP degradation, so it was speculated that the generated free radicals were mainly attached to the surface of the catalyst, and MeOH and TBA were difficult to quench. In order to verify this statement, phenol was added to the reaction system as a quenching agent. The reaction rate constant of phenol with $SO_4^{-\bullet}$ and •OH was high and the polarity was weak, so it could effectively quench the free radicals on the catalyst surface (Yan *et al.* 2017). After the addition of phenol, the degradation efficiency decreased to 51.77%, and the inhibition of CIP degradation by phenol was significantly higher than that by MeOH and TBA, indicating that free radicals were mainly produced on the surface of the catalyst. In addition, NB could be used to quench free radicals on the catalyst surface due to its hydrophobicity. The reaction rate of NB with •OH was 3,000 times that of $SO_4^{-\bullet}$ (fast reaction) (Neta *et al.* 1988). Therefore, the effect of •OH on the catalyst surface could be evaluated by adding NB to this system. The inhibition effect of 100 mM NB on CIP degradation efficiency was much smaller than that of other quenchers, indicating that the main free radical on the catalyst surface was $SO_4^{-\bullet}$ rather than •OH.

It has been reported that the –OH group was essential in the heterogeneous activation of PMS by metal-based catalysts (Liu *et al.* 2015). In order to determine the role of the –OH group on the catalyst surface, KH_2PO_4 was added to the system as a masking agent to study its effect on CIP degradation. KH_2PO_4 could easily combine with transition metals to mask the –OH group on the catalyst surface (Khan *et al.* 2017), preventing the interaction of the –OH group with HSO_5^-. After 10.0 mM $H_2PO_4^-$ was added to the ε-MnO_2/PMS system, the degradation efficiency of CIP decreased from 91.9 to 15.9%, which indicated that the –OH group on the catalyst surface played an important role in controlling the interaction between peroxides and catalysts.

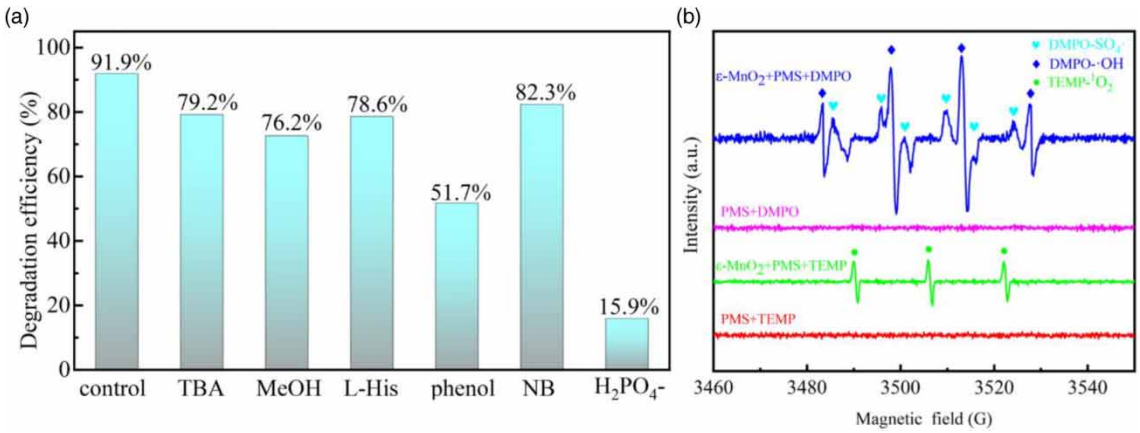

Figure 5 | The degradation of CIP in the presence of MeOH (3 M), TBA (3 M), L-His (0.2 mM), phenol (0.1 M), NB (0.1 M) and $H_2PO_4^-$ (0.01 M) (a) and EPR spectrum of solution, reaction conditions: $[CIP]_0 = 10$ mg/L, [catalyst] = 0.2 g/L, [PMS] = 0.6 g/L, temperature = 25 °C, pH was not adjusted.

To further determine the production of reactive oxygen species, EPR tests were performed on ε-MnO_2/PMS system and PMS system alone using DMPO and TEMP as spin trapping agents. $SO_4^{-\bullet}$ and •OH could form stable adducts with DMPO, which could be detected by electron paramagnetic resonance (EPR) spectroscopy, so DMPO was used as a trapping agent for $SO_4^{-\bullet}$ and •OH, and TEMP was a spin capture agent for $^1O_2$ (Xu *et al.* 2021). As shown in Figure 5(b), the mixed signals of DMPO-$SO_4^{-\bullet}$ and DMPO-•OH and the triplex signal of TEMP-$^1O_2$ (1:1:1) were observed in the spectrum of the ε-MnO_2/PMS system, but no obvious signal was detected when only PMS existed indicating that PMS produced $SO_4^{-\bullet}$, •OH and $^1O_2$ in solution under the activation of ε-MnO_2, and the quantity of $SO_4^{-\bullet}$ was higher than that of •OH and $^1O_2$ in terms of relative spectral intensity.

By comparing the XPS spectra before and after the ε-MnO_2 reaction (Figure 3(a)–3(c)), it was found that the manganese content of different valence states changed, Mn(III) decreased with Mn(IV) increasing, Mn(III)/Mn(IV) decreased from 5.85 to 4.82. The relative content of O_{ads} also decreased, and the O_{ads} of ε-MnO_2 participated in the reaction. The proportion of Mn and O species changed slightly before and after ε-MnO_2 reaction, indicating that ε-MnO_2 could regenerate itself and maintain high activity while participating in the reaction.

Based on the above experimental results, the reaction mechanism of ε-MnO_2-activated PMS to degrade CIP was speculated in Figure 6. On the one hand, PMS combined with ε-MnO_2 in the reaction process, reducing Mn^{4+} to Mn^{3+}, and simultaneously generating $SO_5^{\bullet-}$ (Equation (3)), and Mn^{3+} reacted with PMS to produce $SO_4^{-\bullet}$. In addition, the hydroxyl group on the catalyst surface could act as a bridge between the catalyst and PMS, which could promote the activation of PMS. First, the hydroxyl group combines with Mn^{4+} (Mn^{3+}) to form Mn^{4+} (Mn^{3+}) –OH and Mn^{4+} (Mn^{3+}) –OH reacted with HSO_5^- to form $Mn^{4+}(Mn^{3+}) - HSO_5^-$ (Equation (12)), and then $Mn^{4+}(Mn^{3+}) - HSO_5^-$ was decomposed to form $SO_4^{-\bullet}$ (Equation (13)). $SO_4^{-\bullet}$ could also react with OH^- to form •OH (Equation (14)), and •OH could be decomposed into $^1O_2$ during the dissolution process (Equation (15)). These active substances in the solution eventually attacked the chemical bonds in CIP to make it decomposed and mineralized (Equation (16)). The oxidation–reduction reaction between Mn^{4+} and Mn^{3+} occurred in the catalytic process of MnO_2 (Equations (3) and (4)), and the catalyst reacted and self-repaired simultaneously during the degradation process, which could effectively reduce its wastage and extend its working life. This result was of great significance to the actual water treatment engineering.

$$\equiv Mn^{(4+/3+)} - OH + HSO_5^- \rightarrow \equiv Mn^{(4+/3+)} - HSO_5^- + OH^- \quad (12)$$

$$\equiv Mn^{(4+/3+)} - HSO_5^- + H_2O \rightarrow \equiv Mn^{(3+/4+)} - OH^- + SO_4^{-\bullet} + H^+ \quad (13)$$

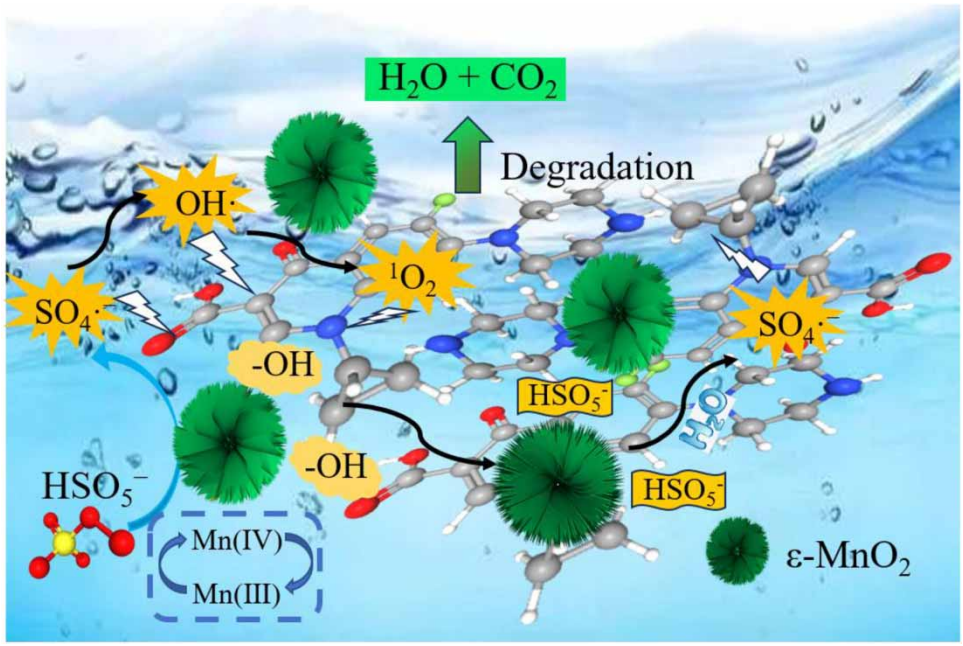

Figure 6 | The mechanism of ε-MnO_2 activating PMS to degrade CIP.

$$SO_4^{-\bullet} + OH^- \rightarrow OH\bullet + SO_4^{2-} \quad (14)$$

$$4OH\bullet \rightarrow {}^1O_2 + 2H_2O \quad (15)$$

$$SO_4^{-\bullet} + \bullet OH + {}^1O_2 + CIP(dissolved) \rightarrow \text{Intermediate products} \rightarrow H_2O + CO_2 + \ldots \quad (16)$$

CONCLUSIONS

An environmentally friendly catalytic material, ε-MnO_2 was synthesized by the redox precipitation method and used to activate PMS to degrade the antibiotic CIP. The results showed that the CIP degradation rate could reach 93% within 30 min after the optimization of reaction parameters. The high activity of ε-MnO_2 was related to its physicochemical properties of the surface, such as the specific surface area, the oxygen vacancy formed by the defect and the Mn(III)/Mn(IV) content ratio. After four cycles of degradation experiments, the efficiency decreased by 13%, which confirmed that the catalyst had good stability. The quenching experiment and EPR result showed that sulfate radicals, hydroxyl radicals and singlet oxygen jointly participated in the degradation of CIP. The main free radical was $SO_4^{-\bullet}$. The hydroxyl group on the surface of ε-MnO_2 was helpful to the contact between PMS and the catalyst, which could promote the activation of PMS. The redox reaction between Mn^{4+} and Mn^{3+} occurred during the activation of PMS by ε-MnO_2, which could realize the self-repair *in situ* and recycle of the catalyst, which provided the theoretical basis and technical support for the removal of antibiotics and had great potential for practical engineering application.

ACKNOWLEDGEMENTS

This study was financially supported by Gansu Province Higher Education Industry Support Plan Project (2022CYZC-40), Natural Science Foundation of Gansu Provincial Department of Science and Technology (22JR5RA316), Major Scientific and Technological Achievements Cultivation Project of Lanzhou Jiaotong University (2022CG07) and Tianyou Innovation Team of Lanzhou Jiaotong University (TY202005).

DATA AVAILABILITY STATEMENT

All relevant data are included in the paper or its Supplementary Information.

CONFLICT OF INTEREST

The authors declare there is no conflict.

REFERENCES

Alhaddad, M. & Amin, M. S. 2022 Removal of ciprofloxacin applying Pt@$BiVO_4$-g-C_3N_4 nanocomposite under visible light. *Optical Materials* **124**, 111976.

Anirudh Gupta, A. G. 2019 Adsorption and oxidation of ciprofloxacin in a fixed bed column using activated sludge derived activated carbon. *Journal of Environmental Management* **250**, 109474.

Arif, M., Liu, G., Zia Ur Rehman, M., Yousaf, B., Ahmed, R., Mian, M. M., Ashraf, A., Mujtaba Munir, M. A., Rashid, M. S. & Naeem, A. 2022 Carbon dioxide activated biochar-clay mineral composite efficiently removes ciprofloxacin from contaminated water – reveals an incubation study. *Journal of Cleaner Production* **332**, 130079.

Chen, Y., Yan, J., Ouyang, D., Qian, L., Han, L. & Chen, M. 2017 Heterogeneously catalyzed persulfate by CuMgFe layered double oxide for the degradation of phenol. *Applied Catalysis A: General* **538**, 19–26.

Chen, X., Oh, W. & Lim, T. 2018 Graphene- and CNTs-based carbocatalysts in persulfates activation: material design and catalytic mechanisms. *Chemical Engineering Journal* **354**, 941–976.

Chun-Hui Shen, X. W. Z. F. 2019 Visible-light-driven activation of peroxymonosulfate for accelerating ciprofloxacin degradation using CeO_2/CO_3O_4 p-n heterojunction photocatalysts. *Chemical Engineering Journal* **391**, 123612.

Enyoh, C. E. & Wang, Q. 2023 Adsorption and toxicity characteristics of ciprofloxacin on differently prepared polyethylene terephthalate microplastics from both experimental and theoretical perspectives. *Journal of Water Process Engineering* **53**, 103909.

Falyouna, O., Maamoun, I., Bensaida, K., Tahara, A., Sugihara, Y. & Eljamal, O. 2022 Encapsulation of iron nanoparticles with magnesium hydroxide shell for remarkable removal of ciprofloxacin from contaminated water. *Journal of Colloid and Interface Science* **605**, 813–827.

Gao, F., Li, Y. & Xiang, B. 2018 Degradation of bisphenol A through transition metals activating persulfate process. *Ecotoxicology and Environmental Safety* **158**, 239–247.

Ghauch, A., Baalbaki, A., Amasha, M., El Asmar, R. & Tantawi, O. 2017 Contribution of persulfate in UV-254 nm activated systems for complete degradation of chloramphenicol antibiotic in water. *Chemical Engineering Journal* **317**, 1012–1025.

Gujar, S. K., Divyapriya, G., Gogate, P. R. & Nidheesh, P. V. 2023 Environmental applications of ultrasound activated persulfate/peroxymonosulfate oxidation process in combination with other activating agents. *Critical Reviews in Environmental Science and Technology* **53**, 780–802.

Hao, S., Yu, M., Zhang, Y., Abdelkrim, Y. & Qu, J. 2019 Hierarchical mesoporous cobalt silicate architectures as high-performance sulfate-radical-based advanced oxidization catalysts. *Journal of Colloid and Interface Science* **545**, 128–137.

He, D., Li, Y., Lyu, C., Song, L., Feng, W. & Zhang, S. 2020 New insights into MnOOH/peroxymonosulfate system for catalytic oxidation of 2,4-dichlorophenol: morphology dependence and mechanisms. *Chemosphere* **255**, 126961.

He, L., Chen, H., Wu, L., Zhang, Z., Ma, Y., Zhu, J., Liu, J., Yan, X., Li, H. & Yang, L. 2021a Synergistic heat/UV activated persulfate for the treatment of nanofiltration concentrated leachate. *Ecotoxicology and Environmental Safety* **208**, 111522.

He, Y., Wang, L., Chen, Z., Shen, B., Wei, J., Zeng, P. & Wen, X. 2021b Catalytic ozonation for metoprolol and ibuprofen removal over different MnO_2 nanocrystals: efficiency, transformation and mechanism. *Sci Total Environ* **785**, 147328.

Hu, X., Hu, X., Peng, Q., Zhou, L., Tan, X., Jiang, L., Tang, C., Wang, H., Liu, S., Wang, Y. & Ning, Z. 2020 Mechanisms underlying the photocatalytic degradation pathway of ciprofloxacin with heterogeneous TiO_2. *Chemical Engineering Journal* **380**, 122366.

Huang, J. & Zhang, H. 2019 Mn-based catalysts for sulfate radical-based advanced oxidation processes: a review. *Environment International* **133**, 105141.

Huang, Y., Huang, Y., Huang, C. & Chen, C. 2009 Efficient decolorization of azo dye reactive black B involving aromatic fragment degradation in buffered CO^{2+}/PMS oxidative processes with a ppb level dosage of CO^{2+}-catalyst. *Journal of Hazardous Materials* **170**, 1110–1118.

Huang, W., Chen, J. & Zhang, J. 2018a Removal of ciprofloxacin from aqueous solution by rabbit manure biochar. *Environmental Technology* **41**, 1380–1390.

Huang, Y., Tian, X., Nie, Y., Yang, C. & Wang, Y. 2018b Enhanced peroxymonosulfate activation for phenol degradation over MnO_2 at pH 3.5–9.0 via Cu(ii) substitution. *Journal of Hazardous Materials* **360**, 303–310.

Huang, J., Dai, Y., Singewald, K., Liu, C., Saxena, S. & Zhang, H. 2019 Effects of MnO_2 of different structures on activation of peroxymonosulfate for bisphenol A degradation under acidic conditions. *Chemical Engineering Journal (Lausanne, Switzerland: 1996)* **370**, 906–915.

Hussain, S., Aneggi, E. & Goi, D. 2021 Catalytic activity of metals in heterogeneous Fenton-like oxidation of wastewater contaminants: a review. *Environmental Chemistry Letters* **19**, 2405–2424.

Issaka, E., Amu-Darko, J. N., Yakubu, S., Fapohunda, F. O., Ali, N. & Bilal, M. 2022 Advanced catalytic ozonation for degradation of pharmaceutical pollutants-a review. *Chemosphere* **289**, 133208.

Jing, D., Yongjian, G., Chaoqun, T., Hongyu, W., Qingsong, L., Shiqing, Z. & Kejia, Z. 2017 Degradation of ciprofloxacin using α-MnO_2 activated peroxymonosulfate process: effect of water constituents, degradation intermediates and toxicity evaluation. *Chemical Engineering Journal* **330**, 1390–1400.

Khan, A., Wang, H., Liu, Y., Jawad, A., Ifthikar, J., Liao, Z., Wang, T. & Chen, Z. 2017 Highly efficient α-mn_2o_3@α-MnO_2-500 nanocomposite for peroxymonosulfate activation: comprehensive investigation of manganese oxides. *Journal of Materials Chemistry A.* **6**, 1590–1600.

Lin, M. & Chen, Z. 2020 A facile one-step synthesized epsilon-MnO_2 nanoflowers for effective removal of lead ions from wastewater. *Chemosphere (Oxford)* **250**, 126329.

Lin, C. & Tsai, C. 2019 Degradation of isopropyl alcohol using UV and persulfate in a large reactor. *Separation and Purification Technology* **209**, 88–93.

Liu, J., Zhao, Z., Shao, P. & Cui, F. 2015 Activation of peroxymonosulfate with magnetic Fe_3O_4-MnO_2 core-shell nanocomposites for 4-chlorophenol degradation. *Chemical Engineering Journal* **262**, 854–861.

Liu, Z., Gao, Z., Xu, L. & Hu, F. 2020 Efficient and rapid adsorption of rare earth elements from water by magnetic Fe_3O_4/MnO_2 decorated reduced graphene oxide. *Journal of Molecular Liquids* **313**, 113510.

Liu, J., An, F., Zhu, C. & Zhou, D. 2021 Efficient transformation of DDT with peroxymonosulfate activation by different crystallographic MnO_2. *Science of the Total Environment* **759**, 142864.

Meng, Y., Song, W., Huang, H., Ren, Z., Chen, S. Y. & Suib, S. L. 2014 Structure-property relationship of bifunctional MnO_2 nanostructures: highly efficient, ultra-stable electrochemical water oxidation and oxygen reduction reaction catalysts identified in alkaline media. *Journal of the American Chemical Society* **136**, 11452–11464.

Nasrollahi, N., Vatanpour, V. & Khataee, A. 2022 Removal of antibiotics from wastewaters by membrane technology: limitations, successes, and future improvements. *Science of the Total Environment* **838**, 156010.

Neta, P., Huie, R. E. & Huie, P. N. A. R. 1988 Rate constants for reactions of inorganic radicals in aqueous solution. *Journal of Physical and Chemical Reference Data* **17**, 1027–1284.

Omuferen, L. O., Maseko, B. & Olowoyo, J. O. 2022 Occurrence of antibiotics in wastewater from hospital and convectional wastewater treatment plants and their impact on the effluent receiving rivers: current knowledge between 2010 and 2019. *Environmental Monitoring and Assessment* **194**, 306.

Rama, P., Roggy, D., Satinder, K. B., Patrick, D., Francois, P., Mausam, V. & Rao, Y. S. 2018 Activation of persulfate by homogeneous and heterogeneous iron catalyst to degrade chlortetracycline in aqueous solution. *Chemosphere* **207**, 543–551.

Ren, Y., Ma, Z. & Dai, S. 2014 Nanosize control on porous β-MnO_2 and their catalytic activity in CO oxidation and N_2O decomposition. *Materials* **7**, 3547–3556.

Salari, M., Nikoo, M. R., Al-Mamun, A., Rakhshandehroo, G. R. & Mooselu, M. G. 2022 Optimizing Fenton-like process, homogeneous at neutral pH for ciprofloxacin degradation: comparing RSM-CCD and ANN-GA. *Journal of Environmental Management* **317**, 115469.

Saputra, E., Muhammad, S., Sun, H., Ang, H. M., Tadé, M. O. & Wang, S. 2013a Different crystallographic one-dimensional MnO_2 nanomaterials and their superior performance in catalytic phenol degradation. *Environmental Science & Technology* **47**, 5882–5887.

Saputra, E., Muhammad, S., Sun, H., Ang, H., Tadé, M. O. & Wang, S. 2013b A comparative study of spinel structured Mn_3O_4, Co_3O_4 and Fe_3O4 nanoparticles in catalytic oxidation of phenolic contaminants in aqueous solutions. *Journal of Colloid and Interface Science* **407**, 467–473.

Shah, S., Rehman, M. U., Arslan, M., Abbasi, S. A., Hayat, A., Anwar, S., Iqbal, S. & Afzal, M. 2022 Response surface methodology for optimization of operational parameters to remove ciprofloxacin from contaminated water in the presence of a bacterial consortium. *ACS Omega* **7**, 27450–27457.

Tian, K., Shi, F., Cao, M., Zheng, Q. & Zhang, G. 2022 A review of persulfate activation by magnetic catalysts to degrade organic contaminants: mechanisms and applications. *Catalysts* **12**, 1058.

Wang, J. & Wang, S. 2018 Activation of persulfate (PS) and peroxymonosulfate (PMS) and application for the degradation of emerging contaminants. *Chemical Engineering Journal* **334**, 1502–1517.

Wang, H., Yin, F., Chen, B. & Li, G. 2015a Synthesis of an ε-MnO_2/metal-organic-framework composite and its electrocatalysis towards oxygen reduction reaction in an alkaline electrolyte. *Journal of Materials Chemistry A* **31**, 16168–16176.

Wang, Y., Indrawirawan, S., Duan, X., Sun, H., Ang, H. M., Tadé, M. O. & Wang, S. 2015b New insights into heterogeneous generation and evolution processes of sulfate radicals for phenol degradation over one-dimensional α-MnO_2 nanostructures. *Chemical Engineering Journal* **266**, 12–20.

Wei, D., Liu, J., Luo, Z. & Xie, X. 2023 Insight into the reactions of antimonite with manganese oxides: synergistic effects of Mn(iii) and oxygen vacancies. *Water Research* **232**, 119681.

Wen-Da, O., Zhili, D. & Teik-Thye, L. 2016 Generation of sulfate radical through heterogeneous catalysis for organic contaminants removal: current development, challenges and prospects. *Applied Catalysis. B, Environmental* **194**, 169–201.

Wilkinsan, F. 1981 Rate constants for the decay and reactions of the lowest electronically excited singlet state of molecular oxygen in solution. *Journal of Physical and Chemical Reference Data* **4** (10), 809–999.

Xu, X., Zhang, Y., Zhou, S., Huang, R., Huang, S., Kuang, H., Zeng, X. & Zhao, S. 2021 Activation of persulfate by MnOOH: degradation of organic compounds by nonradical mechanism. *Chemosphere* **272**, 129629.

Yan, S., Xiong, W., Xing, S., Shao, Y., Guo, R. & Zhang, H. 2017 Oxidation of organic contaminant in a self-driven electro/natural maghemite/peroxydisulfate system: efficiency and mechanism. *Science of the Total Environment* **599–600**, 1181–1190.

Yang, Q., Hou, P., Bai, S., Wang, M. & Cheng, H. 2001 Adsorption and capillarity of nitrogen in aggregated multi-walled carbon nanotubes. *Chemical Physics Letters* **345**, 18–24.

Yoon, S. E., Kim, C. & Hwang, I. 2022 Continuous Fe(ii)-dosing scheme for persulfate activation: performance enhancement mechanisms in a slurry phase reactor. *Chemosphere* **308**, 136401.

Yu, R., Zhao, J., Zhao, Z. & Cui, F. 2020 Copper substituted zinc ferrite with abundant oxygen vacancies for enhanced ciprofloxacin degradation via peroxymonosulfate activation. *Journal of Hazardous Material* **390**, 121998.

Zhang, L., Zhao, X., Niu, C., Tang, N., Guo, H., Wen, X., Liang, C. & Zeng, G. 2019 Enhanced activation of peroxymonosulfate by magnetic Co_3MnFeO_6 nanoparticles for removal of carbamazepine: efficiency, synergetic mechanism and stability. *Chemical Engineering Journal* **362**, 851–864.

Zhang, Y., Zhang, B., Teng, Y., Zhao, J. & Sun, X. 2021 Heterogeneous activation of persulfate by carbon nanofiber supported Fe_3O_4@carbon composites for efficient ibuprofen degradation. *Journal of Hazardous Materials* **401**, 123428.

Zhao, Y., An, H., Dong, G., Feng, J., Wei, T., Ren, Y. & Ma, J. 2020 Oxygen vacancies induced heterogeneous catalysis of peroxymonosulfate by Ni-doped $AgFeO_2$ materials: evolution of reactive oxygen species and mechanism. *Chemical Engineering Journal* **388**, 124371.

Zhen, Y., Sun, Z., Jia, Z., Liu, C., Zhu, S., Li, X., Wang, W. & Ma, J. 2023 Facile preparation of α-MnO_2 nanowires for assembling free-standing membrane with efficient Fenton-like catalytic activity. *Chinese Chemical Letters* **34**, 107664.

Zhou, S., Hu, Y., Yang, M., Liu, Y., Li, Q., Wang, Y., Gu, G. & Gan, M. 2023 Insights into the mechanism of persulfate activation with carbonated waste metal adsorbed resin for the degradation of 2,4-dichlorophenol. *Environmental Research* **226**, 115639.

First received 2 August 2023; accepted in revised form 27 September 2023. Available online 11 October 2023